J. Fluid Mech. (2001), *vol.* 444, *pp.* 79–98. Printed in the United Kingdom

An experimental study of the influence of a rotating magnetic field on Rayleigh–Bénard convection

By M. P. VOLZ AND K. MAZURUK

NASA Marshall Space Flight Center, SD47, Huntsville, AL 35812, USA

(Received 12 November 1999 and in revised form 6 February 2001)

A destabilizing vertical temperature gradient and a rotating magnetic field have been applied to a cylindrical column of liquid gallium. The convective flows which arise as a function of these parameters are identified. For small magnetic field strengths, a regime of stationary flow is observed. This regime is bounded by critical values of the Rayleigh and magnetic Taylor numbers. As the rotating magnetic field is increased, the critical Rayleigh number can increase by more than a factor of 10. The rotating magnetic field itself induces an instability at a critical value of the magnetic Taylor number independent of the Rayleigh number. The nature of the bifurcations (whether subcritical or supercritical) and the convective flows occurring at the critical Rayleigh numbers are dependent upon the magnetic Taylor number. For small magnetic Taylor numbers, the experimental observations are consistent with the occurrence of a single asymmetric meridional roll which is driven around the cylinder by the rotating magnetic field.

1. Introduction

The quality of bulk semiconductor crystals depends on their compositional and structural homogeneity. For crystals grown from the melt, homogeneity is greatly influenced by the convective motions and heat transport occurring during the crystal growth process. The quality of resulting crystals can be diminished when the flow is oscillatory. Flow oscillations couple to the heat transport and cause fluctuations in the growth rate, which in severe instances can lead to periodic solidification and remelt at the interface. The fluctuations often result in visible striations in the grown crystals (Tiller 1991).

One means which crystal growers have employed to control undesirable temperature fluctuations is the use of forced convection. As early as 1961, Chandrasekhar showed that forced convection through fluid rotation can suppress natural convection and increase the critical Rayleigh number (Ra^c) at which temperature fluctuations ensue. In addition to suppressing natural convection, forced convection can also homogenize the fluid, increase the thermal and solutal symmetry in the fluid, and provide a means to control the solid–liquid interface shape. Examples of crystal growth techniques utilizing forced convection are the Czochralski technique and the accelerated crucible rotation technique. An alternative technique which is receiving increasing attention, and the one which is the subject of this paper, is the use of rotating magnetic fields (RMFs).

A RMF interacts with an electrically conducting fluid via the Lorentz force and provides a non-mechanical means of inducing forced convection in the fluid. This

rotational stirring has been used to advantage in industrial applications such as the continuous casting of steel for many years (Birat & Choné 1983; Spitzer, Dubke & Schwerdtfeger 1986). More recently, RMFs have been used to control fluid and heat transport during the growth of semiconductor crystals. Such usage has resulted, in part, from the demonstrated ability of RMFs to homogenize multi-component melts (Gelfgat & Gorbunov 1994) and to control the shape of the liquid–solid interface (Sorkin & Mozgirs 1992). Salk *et al.* (1994) grew CdTe and CdTeSe crystals using the travelling heater method under microgravity conditions. A RMF of 2 mT and 400 Hz was applied during part of the growth. The CdTe crystals had a more homogenous distribution of $\mu\tau$ products and resistivity, and the CdTeSe crystals had fewer deep level defects, increased resistivity, and were better suited as high energy radiation detectors when the field was turned on (Fiederle *et al.* 1996). Brückner & Schwerdtfeger (1994) used a RMF instead of mechanical rotation to successfully grow crystals of copper, germanium and silicon by the Czochralski method. Dold & Benz (1997) greatly reduced the intensity of striations in Bridgman-grown germanium crystals by applying a 2 mT field rotating at 50 Hz.

In order to take full advantage of the benefits that RMFs might have for crystallization processes, it is essential to gain a better understanding of the fundamental fluid mechanics occurring in the system. In particular, it is important to know what the critical values are for the onset of oscillatory flows. Experimental and numerical modelling studies in model fluid systems can help to provide this information. There have been numerous previous studies which have considered flow resulting solely from buoyancy-induced convection, and numerous studies of flow driven by a RMF in isothermal enclosures, but only a few where both a RMF and buoyancy were simultaneously present. In this paper, we present results from a carefully controlled experimental study of the onset of time-dependent flow in a cylindrical container of liquid gallium. The gallium is subjected to both a destabilizing vertical temperature gradient and a horizontal, azimuthally symmetric RMF. The non-dimensional numbers which determine the flow states are the Rayleigh and magnetic Taylor (T_m) numbers. The nature of the flow states is identified by analysing the temperature response of thermistors immersed in the liquid gallium.

Studies of the buoyancy-driven flow of a fluid layer heated from below, also known as Rayleigh–Bénard convection, can be categorized as linear stability analyses, experimental, or numerical investigations. Charlson & Sani (1971) conducted a linear stability analysis and determined the critical Rayleigh number and the nature of the lowest stable flow modes as a function of aspect ratio. Their analysis considered the cases of both an ideally conducting and an ideally insulating cylinder wall. Buell & Catton (1983*a*) used linear stability analysis to find Ra^c for a cylinder wall of arbitrary thermal conductivity. They determined that at the onset of convection the flow was non-axisymmetric for aspect ratios A (height/diameter) greater than about 0.6 and axisymmetric for aspect ratios less than about 0.6. Experimental measurements of oscillatory flows in mercury contained in a long vertical cylinder were made by Verhoeven (1969). Although the predicted onset of non-axisymmetric steady flow was not detected, oscillatory flow was observed at a Rayleigh number about 10% higher than the theoretical value for steady flow. Kamotani *et al.* (1994) measured critical Rayleigh numbers and oscillation frequencies for $1 < A < 3$ and found that the lowest stable flow mode was non-axisymmetric. They also detected a hysteresis in the critical temperature difference at the transition to oscillatory flow. The critical temperature difference required to eliminate oscillations (upon decreasing the temperature difference) was about 1 K lower than that required to induce them (upon

increasing the temperature difference). Müller, Neumann & Weber (1984) studied Rayleigh–Bénard convection in gallium melts and water for $0.5 \leqslant A \leqslant 5$. They identified critical Rayleigh numbers for the transition to steady, oscillatory, and turbulent flow. In agreement with linear stability analysis and experiments (Müller *et al.* 1984), numerical simulations determined that the least-stable flow mode was an axisymmetric toroid for $A = 0.5$ and a non-axisymmetric single roll for $A = 1$ (Neumann 1990).

A RMF applied to an electrically conducting fluid contained in a vertical cylindrical enclosure will result, in general, in a primary azimuthal swirling flow, which induces a centripetal acceleration which is balanced by a radial pressure gradient (Davidson & Hunt 1987). If the cylinder is truncated at one or both ends, the axial variation in pressure will drive a secondary, meridional flow. The precise nature of the flow will depend on a number of system parameters: the magnitude, frequency and number of poles of the applied field; the electrical conductivity of the liquid and cylinder boundaries; the cylinder aspect ratio; and the geometrical placement of the RMF with respect to the cylinder. There have been numerous articles which have theoretically calculated the dependence of flow on one or more of these parameters (see e.g. Abricka, Krüminš & Gelfgat 1997; Witkowski & Marty 1998; Priede & Gelfgat 1998; Spitzer, Reiter & Schwerdtfeger 1994). Using a scaling analysis, Davidson (1992) developed a second-order differential equation which describes the flow distribution in an axisymmetric cavity of arbitrary profile. The analysis is valid in the low-frequency approximation, where the skin depth is larger than the cylinder radius. Also in the low-frequency approximation, numerical analyses have calculated the evolution of flow as a function of field strength (Priede & Gelfgat 1998; Marty *et al.* 1999). These numerical results indicate the existence of three flow regimes: a viscous regime; a stable nonlinear inertial regime; and an unstable regime. A fourth flow regime, occurring at a higher value of T_m and characterized by quasi-stationary stable fluid motion, was identified by Gelfgat & Gorbunov (1994). However, this subject is still under discussion (Marty *et al.* 1999). Experimental measurements on model isothermal fluids have also been reported. The early measurements were made in fluids which were always in the unstable or turbulent regime (Doronin, Dremov & Kapusta 1973; Robinson & Larsson 1973; Gelfgat, Gorbunov & Kolevzon 1993). This is perhaps not surprising as flow instabilities can occur at magnetic fields as low as 0.5 mT in typical experiment conditions (Kaiser & Benz 1998). More recently, Barz *et al.* (1997) measured the spatial dependence of both the azimuthal and meridional flows and compared their results to theoretical predictions.

At very low values of T_m, the flow induced by a RMF is laminar. As T_m increases, the flow velocity increases, and at a critical value of T_m the flow becomes unstable. Richardson (1974) used a stability analysis to calculate this instability for an infinite cylinder and found that at the onset of instability the secondary motions have a multi-cellular structure. The presence of a top and bottom solid layer tends to have a stabilizing influence on the flow as T_m increases with decreasing aspect ratio (Marty *et al.* 1999; Barz *et al.* 1997). For example, in the infinite case, $T_m^c = 2917$, and for $A = 1$, $T_m^c = O(10^5)$. A difference in the two cases is that whereas Richardson calculated the transition from purely azimuthal flow to two-dimensional steady flow, the numerical calculations for finite height measure the transition to unsteady flow. Numerical simulations have also found that at the critical value instability manifests itself in the form of Taylor vortices which are generated in the middle of the cylinder and swept to the ends by the secondary meridional flow (Kaiser & Benz 1998). However, these authors also found that for small aspect ratios, such as $A = 1$, the vortices do not develop fully.

Experimental cylindrical test cells containing liquid gallium have been used to observe flow behaviour under the combined influence of thermal buoyancy and a RMF. A primary result of these studies is that a RMF can dampen time-dependent fluctuations caused by buoyancy-driven convection (see e.g. Dold & Benz 1997; Fischer *et al.* 1999*a*). Fischer *et al.* (1999*b*) defined an interaction parameter N as the ratio of the magnetic Taylor number and the Grashof number. They found that for $N < 0.03$ large-scale temperature fluctuations occur, while for $N > 0.03$ the fluctuation amplitudes are greatly reduced. Dold & Benz (1999) also examined the transition from flow dominated by a RMF to flow dominated by buoyancy convection. Over the range of Rayleigh numbers investigated, $4.7 \times 10^5 \leqslant Ra \leqslant 1.1 \times 10^6$, they found that the Rayleigh number at which the transition occurs is proportional to the square of the magnetic Taylor number. The nature of the flow has been inferred experimentally by recording the signal from thermal sensors immersed in the liquid gallium (Volz & Mazuruk 1996; Fischer *et al.* 1999*b*). When $Ra > Ra^c$, buoyancy flow is driven around the cylinder in the azimuthal direction and the response of thermal sensors to such a flow has been described by Fischer *et al.* (1999*b*) as thermal waves. Theoretically, it has been shown that as the driving force of a RMF increases, Ra^c increases (Volz & Mazuruk 1999). Therefore, if $T_m < T_m^c$, a thermally unstable flow can be stabilized by applying a RMF of sufficient magnitude.

Studies which have considered the combined effect of both a RMF and buoyancy on fluid behaviour have focused primarily on the effect of a RMF on fluids which are above either Ra^c or T_m^c. They have concentrated on how the amplitude and frequency of oscillations depend on Ra and T_m. However, as the experimental results presented in this paper demonstrate, there is a region in T_m–Ra parameter space where no time-dependent temperature oscillations are observed. This region is bounded by Ra^c and T_m^c. The important question of how a RMF affects Ra^c has not been sufficiently addressed. In only one previous work were the limits of stability in T_m–Ra parameter space experimentally identified (Volz & Mazuruk 1996). However, in that work the temperature gradient applied to the cylinder was continuously changed, resulting in a hysteresis at the bifurcation points. Here we present quantitative measurements of flow states obtained with constant external boundary conditions. The measurements cover the range in T_m–Ra phase space up to and including where time-dependent flow occurs. They also include the endpoint limits of the parameter space, where either Ra or $T_m = 0$. Measurements made at these limits, in the classical Rayleigh–Bénard convection or RMF-dominated forced convection regimes, are compared to previous results in the literature.

2. Experiment apparatus and procedures

2.1. *Experiment apparatus*

The experiments were conducted in a cylindrical vertical enclosure with liquid gallium as the working fluid. The top and bottom of the cell were made from thin (1.5 mm) copper disks and the walls of the cell were constructed of 4 mm thick methyl methacrylate polymer (PMMA). The distance between the top and bottom disks is 24 mm. The inner diameter of the cell is also 24 mm so that the cell has an aspect ratio (height/diameter) of 1. The thermal conductivity of liquid gallium is more than 100 times higher than the PMMA container and hence the sidewalls provide a very good approximation to rigid adiabatic boundary conditions. The temperatures at the top and bottom of the cell are controlled by fluid (ethylene glycol) recirculating from

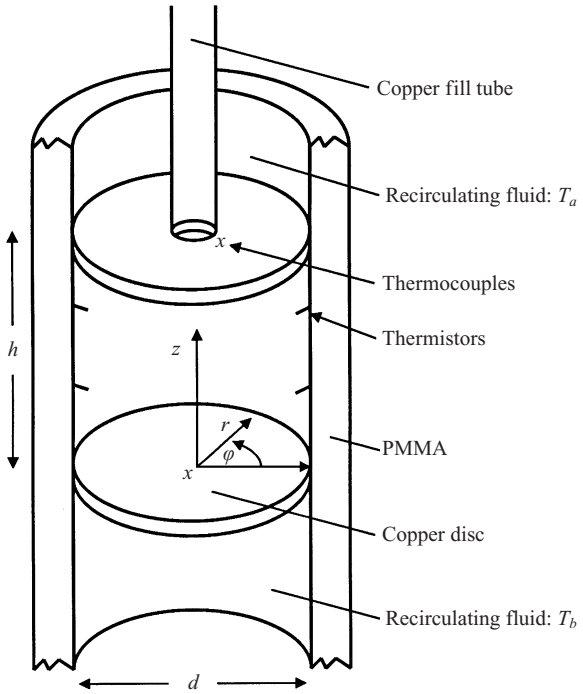

FIGURE 1. Schematic diagram of the experiment apparatus. The liquid gallium is contained between the thin copper disks. Temperatures at the top and bottom of the enclosure are measured with thermocouples embedded in the copper disks and the gallium temperatures are measured with 8 thermistors inserted into the liquid.

Neslab RTE-211 refrigerated bath/circulators. The cell was isolated from possible vibrations from the fluid pumps by having the fluid flow through passive pressurized containers placed between the pumps and the test cell. Thermal interactions with the ambient environment were minimized by packing quartz wool around the liquid gallium cell and the fluid chambers at the top and bottom of the cell. The thermal conductivity of the copper disks is $401\,\mathrm{W\,mK^{-1}}$ (Lide 1999) which is approximately 10 times higher than that of liquid gallium over the range of temperatures at which the experiments were conducted. Thus, the copper disks efficiently conduct heat from the recirculating fluid chambers and provide a uniform temperature surface to the liquid gallium. The liquid gallium was placed in the cell through a thin copper fill-tube with an opening such that more than 97% of the upper gallium surface remained covered by the top copper disc. Gallium was left in the fill-tube to a height of several cm above the liquid cell to ensure that the top surface of gallium in the cell remained in contact with the copper disc. A schematic diagram of the test cell is shown in figure 1.

The fluid dynamics in the cell were inferred from the temperature response of eight thermistors (Thermometrics model P25) inserted into the gallium. Four of the thermistors, labelled L_1 to L_4, were positioned at one third the distance from the bottom to the top of the cell, $z = h/3$. The other four thermistors, labelled U_1 to U_4, were positioned at $z = 2h/3$ with the same azimuthal positions as the lower four thermistors, $\varphi = 0$, $\pi/2$, π and $3\pi/2$. The thermistors protruded 2 mm into the liquid and were 0.6 mm in diameter. The thermistors were operated with a constant current of $10\,\mu\mathrm{A}$ which generated negligible self-heating in the system. The top and bottom

cell temperatures were measured by K-type (chromel-alumel) thermocouples placed in the copper disks less than 0.5 mm from the gallium surfaces. The thermocouples and thermistors were calibrated by measuring the voltages under isothermal conditions at several temperatures spanning the temperature range of interest. The voltage signals were digitized using a 16-bit analog to digital converter and stored on disk to be processed by a personal computer. The peak-to-peak noise fluctuations from the thermistors immersed in gallium were less than 0.005 K.

The cell was placed inside the stator of a two-pole, three-phase electric motor with an inner diameter of 10 cm. The stator generates a magnetic field which rotates in the azimuthal direction with a frequency of 60 Hz. The voltage applied to each of the three phases could be independently controlled to ensure that the magnetic field was azimuthally uniform. The spatial distribution of the magnetic field without the gallium cell present was measured with a Hall probe. The maximum variations in field strength over the dimensions of the gallium cell were less than 4% and the applied magnetic field can be described by

$$\boldsymbol{B} = B\cos(\varphi - \omega t)\boldsymbol{e}_{\mathrm{r}} + B\sin(\varphi - \omega t)\boldsymbol{e}_{\varphi}, \tag{2.1}$$

where B and ω are the magnitude and frequency of the applied magnetic field. When the gallium cell is present, the penetration of the field into the gallium is determined by the skin depth, $\delta = \sqrt{2/\sigma\omega\mu}$, where σ is the electrical conductivity and μ is the magnetic permeability. In the present set-up, the skin depth is greater than the cell radius with $\delta/r_0 = 2.8$. The magnetic field strength in the centre of the cell is reduced with respect to that at the wall although this reduction is expected to be less than 0.1% (Volz & Mazuruk 1999). The induced electric current and Lorentz force depend on the electrical boundary conditions of the cell. Specifically, the degree of electrical connection between the gallium and copper can influence the resultant force, although this effect will be less at lower frequencies. A thin oxide layer forms at the copper–gallium boundaries and the contact resistant across such a layer was measured. For the voltage levels induced by the RMF, this layer is electrically insulating and the induced electric current is thus confined to the gallium.

2.2. *Experiment procedures*

The convective flow states were measured as a function of the Rayleigh and magnetic Taylor numbers. The Rayleigh number is defined as

$$Ra = \frac{g\alpha(T_b - T_a)h^3}{\kappa\nu}, \tag{2.2}$$

where g is the acceleration due to gravity, $9.8\,\mathrm{m\,s^{-2}}$, α is the volumetric thermal expansion coefficient, $T_b - T_a$ is the difference in temperature between the bottom and top of the cell, h is the cell height, κ is the thermal diffusivity and ν is the kinematic viscosity. The magnetic Taylor number is defined as

$$T_m = Ha^2 Re_\omega, \tag{2.3}$$

where Ha is the Hartmann number, Re_ω is the rotational Reynolds number,

$$Ha = r_0 B\sqrt{\frac{\sigma}{2\rho\nu}}, \quad Re_\omega = \frac{\omega r_0^2}{\nu}, \tag{2.4}$$

and ρ is the density. The factor $\sqrt{1/2}$ in the Hartmann number originates from the time-averaged RMF. These non-dimensional numbers depend upon the thermophysical properties of liquid gallium which are, in general, temperature-dependent. The

Symbol	Property	Value (323 K)	Units	References
α	thermal expansion	1.02×10^{-4}	K^{-1}	Lide (1999)
ρ	density	6.067×10^{3}	$kg\,m^{-3}$	Lide (1999)
κ	thermal conductivity	26.8	$W\,mK^{-1}$	Brandes & Brook (1992)
c_p	heat capacity	395.4	$J\,kg^{-1}K^{-1}$	Iida & Guthrie (1988)
$\kappa = k/c_p\rho$	thermal diffusivity	1.12×10^{-5}	$m^2\,s^{-1}$	Lide (1999), Brandes & Brook (1992), Iida & Guthrie (1988)
$v = \eta/\rho$	kinematic viscosity	3.19×10^{-7}	$m^2\,s^{-1}$	Brandes & Brook (1992), Lide (1999)
σ	electrical conductivity	3.82×10^{6}	$S\,m^{-1}$	Iida & Guthrie (1988)

TABLE 1. Properties of liquid gallium at 323 K.

thermophysical property values used in this work and the sources from which they were obtained are shown in table 1. The density (Lide 1999), viscosity (Brandes & Brook 1992), and heat capacity and electrical conductivity (Iida & Guthrie 1988) were calculated from formulas explicitly describing the temperature dependence of these properties. The volumetric thermal expansion coefficient (Lide 1999) is assumed to be temperature independent and the thermal conductivity is calculated from a linear interpolation of values found in Brandes & Brook (1992). The thermal diffusivity and kinematic viscosity are derived from the other properties. All of the results reported in this work were obtained with a mean cell temperature of between 313 and 343 K. The thermophysical properties were approximated to be constant over this range and variations in the Rayleigh and Hartmann numbers result only from changes in the applied temperature differential and applied magnetic field respectively.

Steady-state and dynamic measurements were made in the system. Steady-state measurements are defined as those where the magnetic field and temperatures of the top and bottom zones were set and then the system was allowed to equilibrate. The system was allowed to stabilize for at least one hour before measurements were taken. Changes in temperature to a new setting were slow enough that the temperature profile in the cell remained linear. This quasi-static condition (Müller & Neumann 1983) is met as long as the time taken to change the temperature by 1 K is more than $h^2/2\kappa$. In the present experiments, $h^2/2\kappa = 25.7$ s and this criterion is easily met. The data points which make up the stability diagram were all obtained utilizing the steady-state measurement method. Dynamic measurements were also made. In this method the setpoint of the recirculating bath controlling the temperature at the top of the cell (T_a) was kept fixed and the temperature at the bottom of the cell (T_b) was slowly raised or lowered at a rate typically less than $1\,K\,h^{-1}$. This method allowed the transitions between flow states to be more clearly visualized.

3. Results

The essential results of this study are contained in the magnetic Taylor number–Rayleigh number space diagram shown in figure 2. Five dynamically distinct regimes of flow are identified. The different regimes are experimentally distinguished by the temporal response of the thermistors. In general, the response of a given thermistor was the same as the other 7, with the possible exception of a phase shift between them. No spatially local modes were observed but rather the system oscillated with a

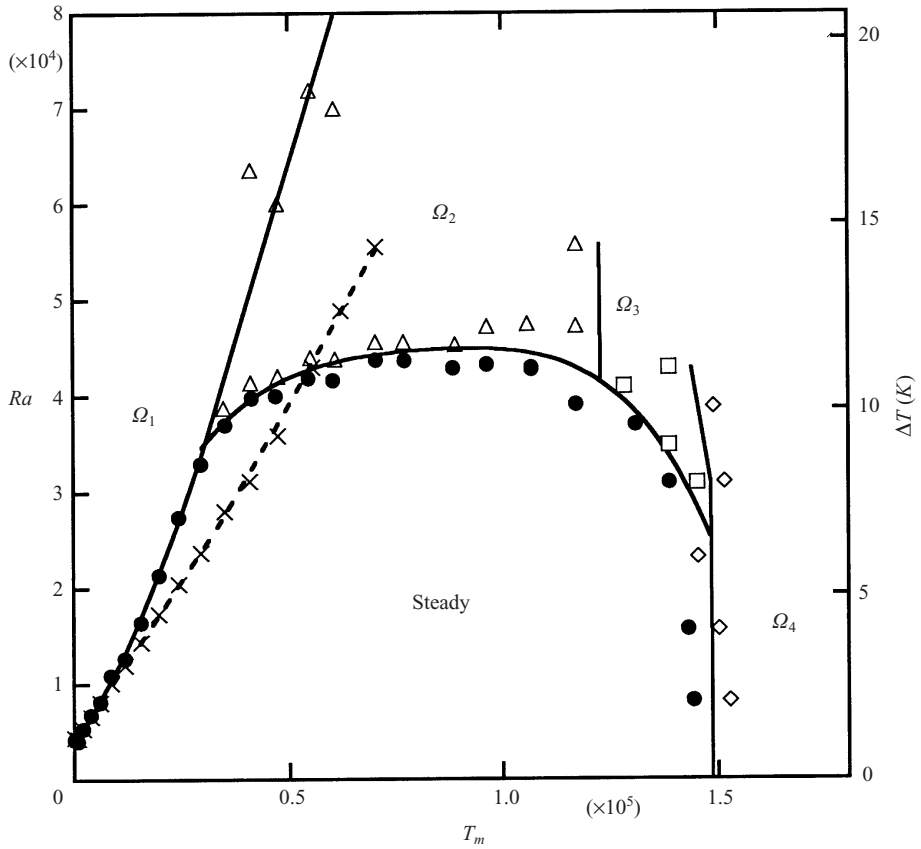

FIGURE 2. Observed dynamical flow states in T_m–Ra parameter space. The regimes labelled Ω_1, Ω_2, Ω_3 and Ω_4 are associated with flow states observed close to the steady region. The solid and dashed lines are drawn as a guide to the eye.

global nature. It must be emphasized that the regions of the T_m–Ra phase diagram labelled Ω_1, Ω_2, Ω_3 and Ω_4 are associated with flow patterns observed immediately adjacent to the steady flow regime. The flow patterns can change as the distance from the steady regime increases. For example, Ω_1 is characterized by a single frequency. As Ra increases, more frequencies appear and eventually turbulence ensues. As the primary objective of this work is to identify the region in T_m–Ra space where the flow is steady and perhaps most favourable for crystal growth, the rich and complex flow dynamics occurring at larger values of Ra and T_m was not fully explored.

The symbols in figure 2 are the measured regimes of flow closest to the bifurcation points. The solid circles are the largest values of Ra where the flow was steady. The crosses are the lowest values of Ra where the flow was of type Ω_1. The hysteresis behaviour between the steady and Ω_1 regimes will be described later in this section. The open triangles, squares and diamonds bound the regimes where, respectively, oscillations of type Ω_2, Ω_3 and Ω_4 were observed. The dashed and solid lines are drawn only as a guide to the eye.

The steady flow regime is defined as that regime where no time-dependent signals from any of the thermistors were observed. Indeed, the regime of steady flow cannot be experimentally distinguished from the condition of no flow. However, for $T_m > 0$, there is flow in the system. No critical value for the onset of flow driven by a RMF

is expected. Previous calculations (i.e. Davidson 1992; Priede & Gelfgat 1998) and experiments (Barz *et al.* 1997; Ramachandran & Mazuruk 1998) have identified the main characteristics for this flow. The primary motion is an azimuthal swirling flow. The azimuthal flow is zero at $r = 0$, reaches a maximum at a value of r determined by the skin depth and Ha, and is zero again at the sidewall. This azimuthal flow causes a radial pressure gradient. For a cylinder of finite height, the radial pressure gradient induces a secondary flow consisting of two axisymmetric meridional rolls. At the midplane of the cylinder, fluid flows outward toward the cylinder wall. It then moves upwards (downwards) towards the top (bottom) of the cell and back down (up) the centre to the midplane.

Classical Rayleigh–Bénard convection occurs in the cell when $T_m = 0$. Experiments with the magnetic field turned off were conducted in order to make comparisons with previous theoretical predictions. Utilizing dynamic measurements (slowly and continuously changing the temperature differential), the transition from the state of no flow to that of flow can easily be identified (Volz & Mazuruk 1996). This is done by plotting the difference in temperature signals of thermistors situated directly across the cell from each other (for example, U_3–U_1 and U_4–U_2). When flow occurs, one or more of the temperature differences becomes non-zero. For a cell with an aspect ratio of 1, the flow which occurs above Ra^c is in the form of a single non-axisymmetric meridional roll (a roll in the r, z plane) (Neumann 1990). The warmer fluid flows up one side of the container and the colder fluid flows back down the other side. This flow is degenerate with respect to φ, and small variations in the experimental conditions determine which value of φ lies along the rotation axis of the roll. In the present work, Ra^c was determined to be 3800. This is in agreement with the value of 3800 obtained in a similar facility by the present authors in an earlier work (Volz & Mazuruk 1996). It also agrees with the value of 3800 obtained from numerical calculations (Neumann 1990), and the value of 3610 obtained from linear stability analysis (Buell & Catton 1983*b*).

Figure 3 shows the dynamic transition between steady flow and Ω_1 oscillations. The differences in temperature seen by thermistors situated 180° across the cell from each other are plotted versus time. The data were obtained with $T_m = 510$, which corresponds to $B = 0.145\,\mathrm{mT}$. At Ra^c, a single non-axisymmetric roll develops in the cell just as it did when $T_m = 0$. However, now there is an azimuthal force which drives the thermal roll around the cylinder. The total flow is a combination of buoyancy flow and RMF-induced flow. In figure 4 the temporal response of thermistors to Ω_1 flow oscillations are shown for a constant value of $Ra > Ra^c$. They are consistent with the picture of a single non-axisymmetric roll rotating around the cylinder. When L_1 is a maximum, L_3 is a minimum, and there is a 90° phase shift between the nearest-neighbour thermistors. The upper thermistor signals follow the same pattern, and the upper and lower thermistors are in phase with each other so that, for example, U_1 is a maximum when L_1 is a maximum. These experimental results are qualitatively consistent with recent calculations (Volz & Mazuruk 1999) which showed that the lowest unstable flow mode is non-axisymmetric and that Ra^c increases with increasing T_m.

A measure of how well the actual experimental conditions approach ideal conditions can be obtained by observing the azimuthal rotation of the thermal roll at very low magnetic field strengths. Deviations from ideal conditions can result, for example, from a misalignment of the vertical axis of the cell with respect to the gravity vector or from slight asymmetries in the thermal field at the top or bottom of the cell. Figure 5 shows the transition from steady flow to Ω_1 oscillations for $B = 0.1\,\mathrm{mT}$,

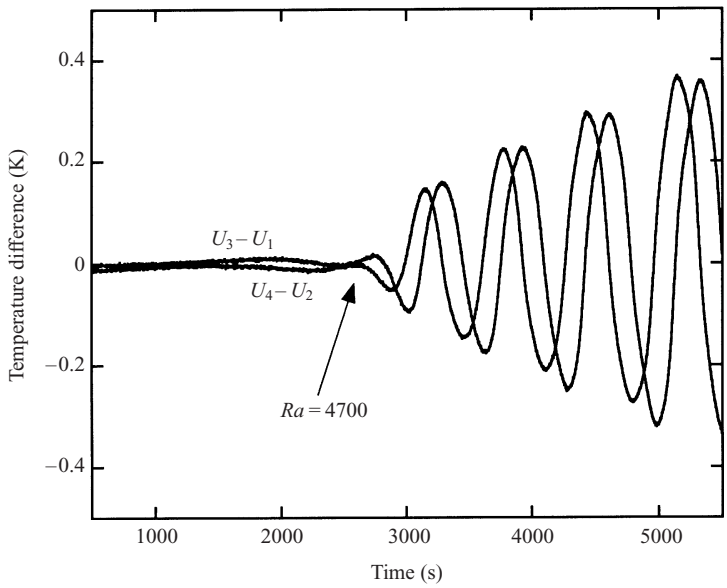

FIGURE 3. Dynamic flow transition between the steady and Ω_1 flow regime. U_3–U_1 and U_4–U_2 are the difference in temperatures between thermistors situated directly across the test cell from each other. The difference in temperature between the top and bottom of the cell increased from 0.54 to 1.81 K during the time shown. $T_m = 510$.

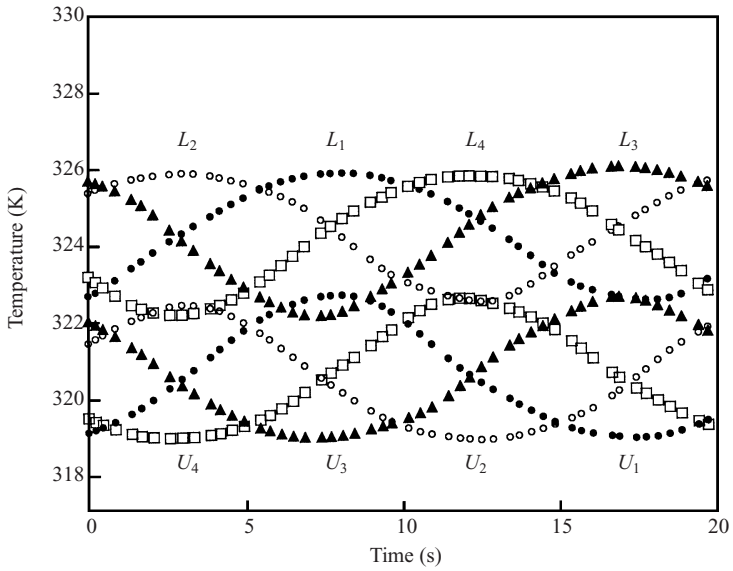

FIGURE 4. Temporal response of thermistors to Ω_1 flow oscillations for $Ra = 35\,900$ and $T_m = 4.8 \times 10^4$.

which corresponds to $T_m = 250$. At this low magnetic field, it takes approximately 2 hours for the thermal roll described earlier to rotate around the cell a single time. This corresponds to an azimuthal velocity of the roll on the order of $10\,\mu\mathrm{m\,s^{-1}}$. Note that this is the velocity of the thermal roll and not the azimuthal fluid velocity, which is a function of r and is not directly measured. Above Ra^c, the meridional flow

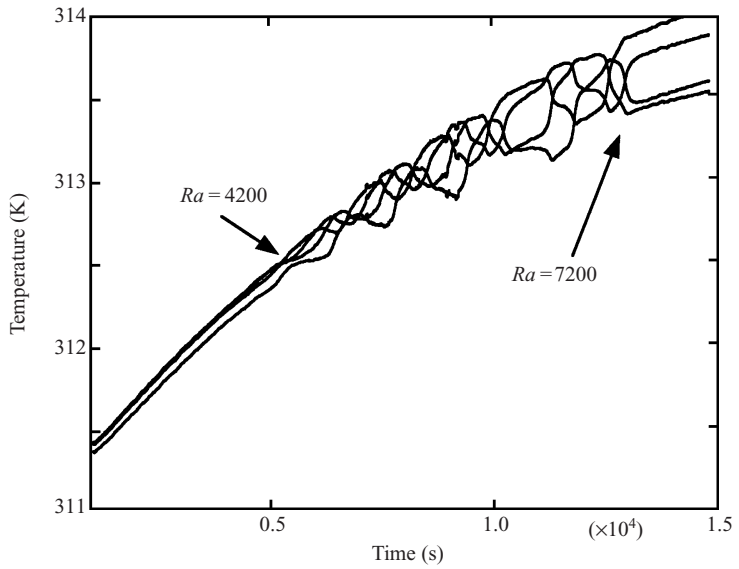

FIGURE 5. Temperatures of the L_1, L_2, L_3 and L_4 thermistors versus time at $T_m = 250$. The temperature differences between the top and bottom of the cell are continuously increased with time. $Ra^c = 4200$ is the critical value for the onset of buoyancy-driven meridional flow. At $Ra = 7200$, buoyancy convection dominates and the thermal roll ceases to rotate around the cylinder.

velocity, driven by thermal buoyancy, is expected to be considerably larger. As can be seen in the figure, the signals deviate from sinusoidal behaviour with increasing Ra. Small deviations from conditions of pure azimuthal symmetry cause there to be a preferred axis of alignment for the thermal roll. As Ra increases, the tendency of the thermal roll to stick to a preferred alignment increases. Finally, at $Ra = 7200$ the driving force for buoyancy convection is strong enough to completely dominate the force driving azimuthal flow and the thermal roll ceases to rotate around the cell. The thermistor signals are then identical to those seen in the Rayleigh–Bénard configuration when $T_m = 0$. The cessation of the azimuthal rotation of the thermal roll, as a result of an increase in Ra, was not seen for $B > 0.1$ mT.

Immediately above the bifurcation from steady flow, the Ω_1, Ω_2 and Ω_3 oscillations are each characterized by a single frequency. These frequencies are independent of $Ra - Ra^c$ near the point of bifurcation, which is a characteristic of Hopf bifurcations (Bergé, Pomeau & Vidal 1986). As $Ra - Ra^c$ is further increased, second- and higher-order critical values of Ra are reached, and multiple frequencies are observed. The frequencies are a function of T_m and their dependence on T_m is shown in figure 6. The frequencies vary by over 3 orders of magnitude. In addition to frequency, a second distinguishing characteristic of the flow modes is the phase relationship between the thermistor signals. These phase relationships are shown in figure 7. There is a 90° phase shift between nearest-neighbour thermistors in Ω_1. The Ω_2 frequency is more than 4 times greater than Ω_1, and there is a 180° phase shift between thermistors. The transition from Ω_2 to Ω_3 involves another discontinuous jump in frequency, and a 90° phase shift is observed in Ω_3. The thermistor signals in Ω_4 are not singly periodic and only the L_1 signal is shown in figure 7(*d*).

The physical interpretation of the Ω_1 oscillation has been described earlier in this section as a buoyancy-driven non-axisymmetric thermal roll which is driven around the cylinder by the RMF. As T_m increases, the force generated by the RMF

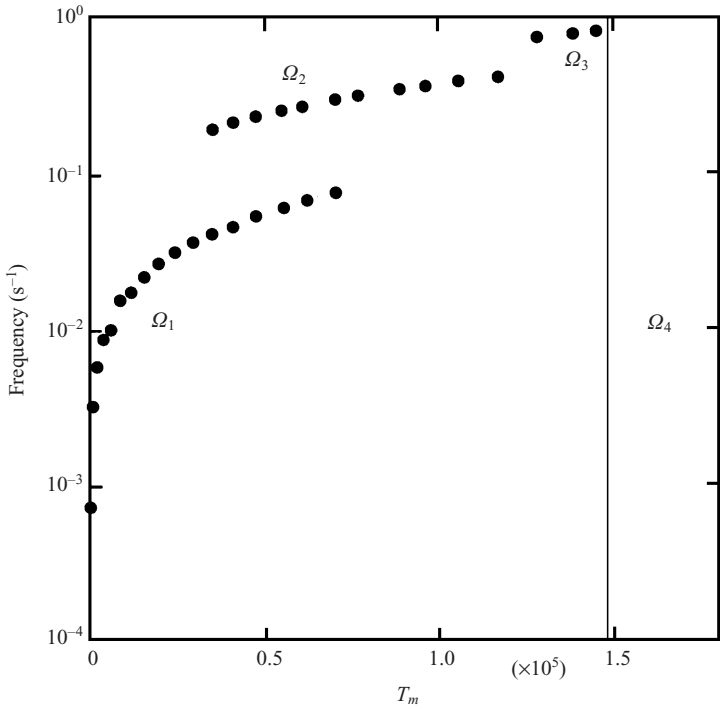

FIGURE 6. Frequencies of flow oscillations versus T_m. The data were obtained just above the transition from the steady regime. In the Ω_1, Ω_2 and Ω_3 flow regimes the oscillations are singly periodic nearest the steady regime. Multiple frequencies are observed in the Ω_4 regime.

increases, and the thermal roll rotates more quickly around the cylinder. Although the average azimuthal fluid velocity and the azimuthal velocity of the thermal roll rotation are generally of the same order of magnitude, they are not identical. Recent calculations have shown that the azimuthal velocity of the thermal roll depends not only on the Hartmann number, but on the skin depth and Prandtl number as well (Volz & Mazuruk 1999). Based on the present experimental data, a definitive physical model of the flow corresponding to the Ω_2, Ω_3 and Ω_4 oscillations is not obvious. If axisymmetric modes do not couple as readily to the RMF as non-axisymmetric modes, as is the case for an infinite cylinder (Volz & Mazuruk 1999), then the most unstable time-independent flow state above a certain value of T_m is axisymmetric. However, the axisymmetric mode cannot be experimentally detected. The Ω_2 oscillations may correspond to a secondary bifurcation to a time-dependent mode above the axisymmetric one but numerical calculations utilizing the appropriate experimental parameters are required to verify this possibility.

The RMF is clearly the dominant driving force for Ω_4 oscillations. The onset of Ω_4 oscillations is independent of *Ra*, and occurs at a critical value of $T_m^c = 1.5 \times 10^5$. The same value of T_m^c was also found in the experiment cell when a stabilizing temperature gradient was applied. Recent calculations have predicted that above T_m^c, instabilities are expected to occur in the form of Taylor vortices which are generated in the middle of the cylinder and transported to the endwalls by the secondary, meridional flow (Kaiser & Benz 1998). The generation of these vortices is expected to be statistical, resulting in non-periodic temperature oscillations. However, the calculations also found that for small aspect ratios, such as that used in the present experiment, the

Reference	T_m^c
Gelfgat & Gorbunov (1994), numerical	1.6×10^5
Barz *et al.* (1997), numerical	2.8×10^5
Kaiser & Benz (1998), numerical	5.4×10^4
Priede & Gelfgat (1998), numerical	4.5×10^5
Marty *et al.* (1999), numerical	1.8×10^5
Mößner & Gerbeth (1999), numerical	2.0×10^5
This work, experimental	1.5×10^5

TABLE 2. Comparison of the critical magnetic Taylor number T_m^c obtained by different authors.

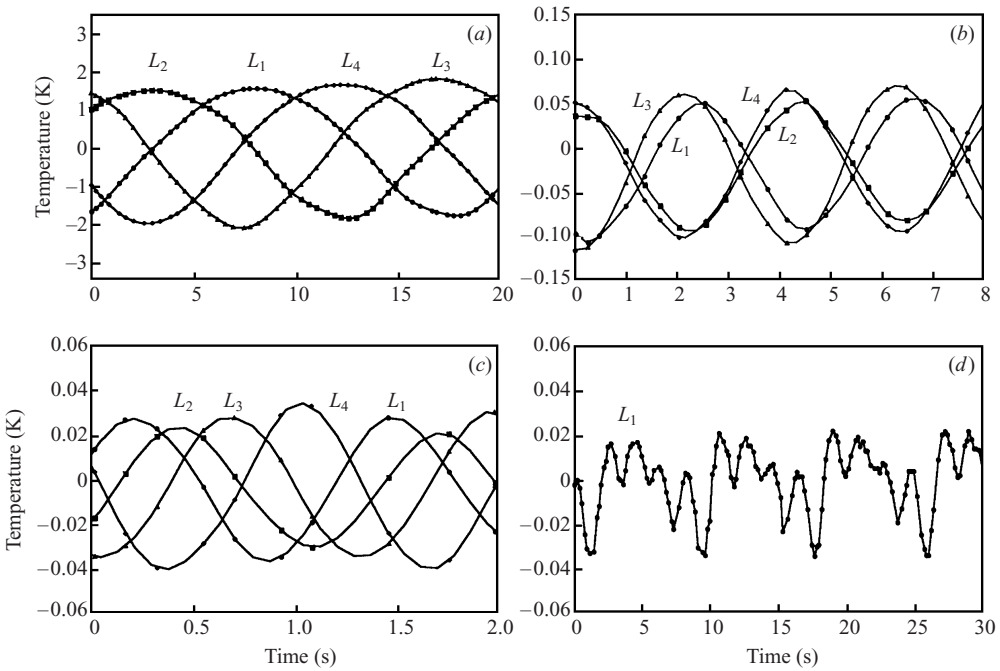

FIGURE 7. Phase relationships between the L_1, L_2, L_3 and L_4 thermistor signals for the (*a*) Ω_1 ($T_m = 4.8 \times 10^4$, $Ra = 35\,900$), (*b*) Ω_2 ($T_m = 4.8 \times 10^4$, $Ra = 42\,000$) and (*c*) Ω_3 ($T_m = 1.4 \times 10^5$, $Ra = 42\,800$) flow regimes. Only the L_1 thermistor signal is shown for the (*d*) Ω_4 ($T_m = 1.5 \times 10^5$, $Ra = 31\,000$) regime.

vortices do not fully develop. For a larger aspect ratio cylinder, a statistical generation of vortices might result in a decreasing correlation of signal with increasing distance from the cylinder midplane. Correlation functions for thermistor signals in the Ω_4 regime are shown in figure 8. Neither the autocorrelation function of the L_1 signal nor the correlation functions of L_1 with other thermistor signals show a significant decay. This indicates that the signals are periodic and correlated, and a decrease in correlation with time, which might be expected to occur in cylinders of larger aspect ratio, is not observed.

A comparison of the current measurement of T_m^c with previous numerical calculations is given in table 2. There is about a factor of 8 difference between the highest and lowest reported values. Direct simulation of T_m^c is a difficult task and there are several possible reasons to account for the spread in the reported values. As Mößner

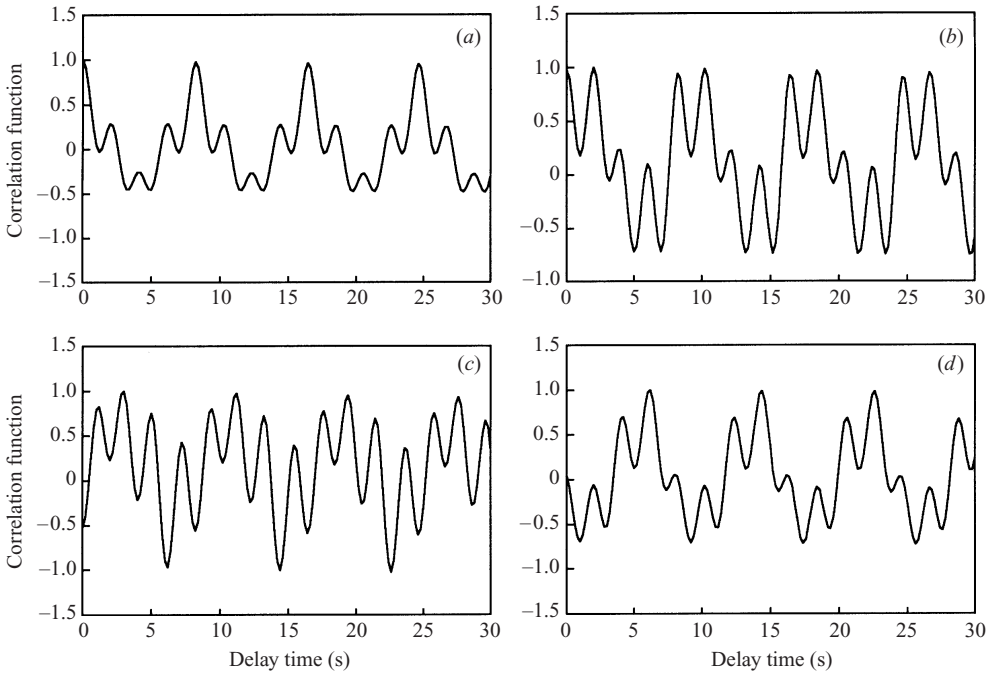

FIGURE 8. Correlation functions for the thermistor signals in the Ω_4 regime. (*a*) L_1L_1, (*b*) L_1U_1, (*c*) L_1L_2, (*d*) L_1L_3.

& Gerbeth (1999) have noted, an accurate calculation requires a minimum number of grid points. Also, near the instability threshold the instabilities develop slowly and an insufficient calculation time may result in an unstable flow being classified as stable. Results may also differ depending on the convergence criterion selected and the direction of approach to the stability limit. For example, Marty *et al.* (1999) found an 80% difference in T_m^c for $A = 5$ depending on whether T_m was decreased from an unstable range until it was stable or whether T_m was increased from a stable range until instability occurred. The physical model chosen can also have an effect. For example, using the infinite cylinder model for the Lorentz force results in a significant underestimate of T_m^c (Kaiser & Benz 1998; Mößner & Gerbeth 1999), although none of the references cited in table 2 used such an approximation. T_m^c can also be affected by the value of Re_ω. Although $T_m = Ha^2 Re_\omega, Re_\omega$ appears independently in the equation for the Lorentz force. Mößner & Gerbeth (1999) found that T_m^c depends weakly on Re_ω, such that T_m^c varies by a factor of 1.6 when Re_ω is allowed to vary over the typical experimental range $10^4 \leqslant Re_\omega \leqslant 10^6$.

A significant hysteresis exists between the steady flow regime and the Ω_1 regime. The bifurcation diagram for these two regimes is shown in figure 9 for $T_m = 3 \times 10^4$. The solid lines connect the experimental data points and the arrows indicate the direction of the transitions. The diagram is characteristic of a subcritical bifurcation. The largest value of Ra for which the flow is steady is $Ra^c = 32\,900$ and the smallest value for which Ω_1 oscillations exist is $Ra^{c\prime} = 23\,600$. Between $Ra^{c\prime}$ and Ra^c, the existence of either steady flow or Ω_1 oscillations depends on the history of the system. The Ω_1 oscillations appear with a finite amplitude and with a frequency that is essentially independent of Ra. However, the frequency did increase slightly with increasing Ra, and a maximum increase of about 10% was observed over the range of data presented

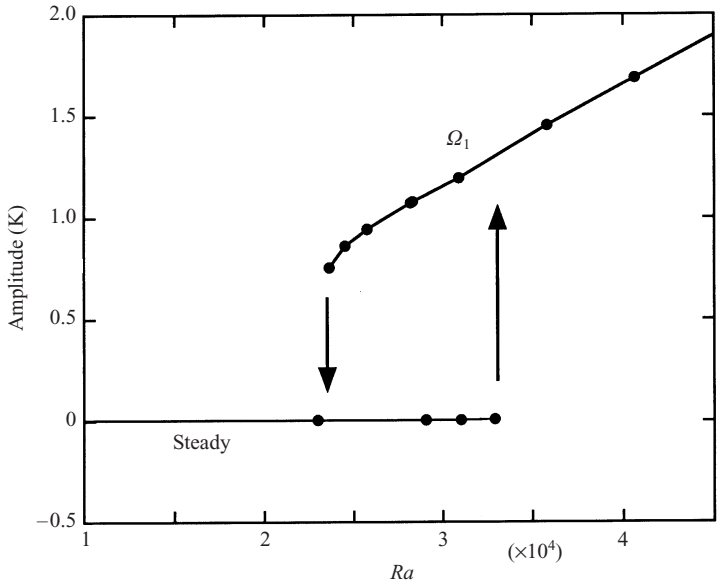

FIGURE 9. Amplitude of flow oscillations versus *Ra*. This bifurcation diagram indicates the hysteresis behaviour between the Ω_1 and steady flow regimes at $T_m = 3.0 \times 10^4$.

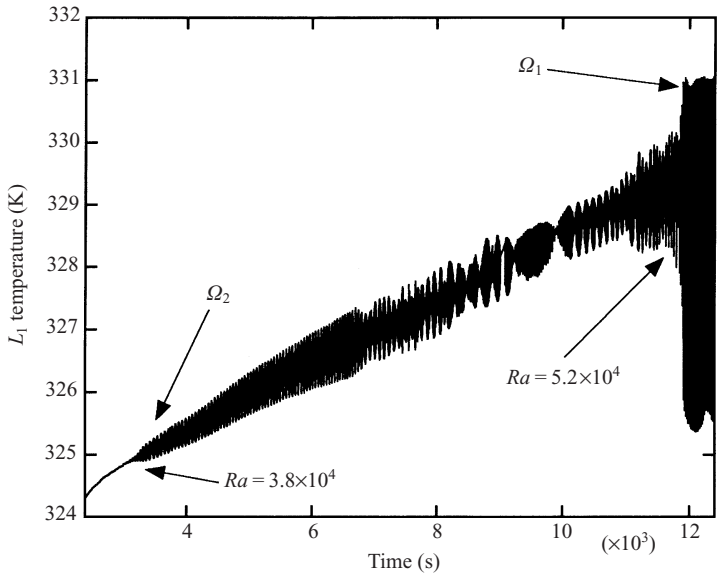

FIGURE 10. L_1 thermistor temperature versus time at $T_m = 5.0 \times 10^4$. The dynamic measurement data indicate the transition to the Ω_2 flow state at $Ra = 3.8 \times 10^4$ and the transition to the Ω_1 flow state at $Ra = 5.2 \times 10^4$.

in figure 9. As shown in figure 2, no hysteresis is observed between the steady and Ω_1 flow regimes when $T_m = 0$. When the RMF is applied to the Rayleigh–Bénard cell such a hysteresis does develop, and $Ra^c - Ra^{c\prime}$ increases as T_m increases. No other hysteresis patterns were observed in transitions between the other flow regimes.

Figure 10 shows the evolution of a thermistor signal as ΔT is continuously increased for a fixed value of $T_m = 5.0 \times 10^4$. Because ΔT is continuously increasing, the fluid is

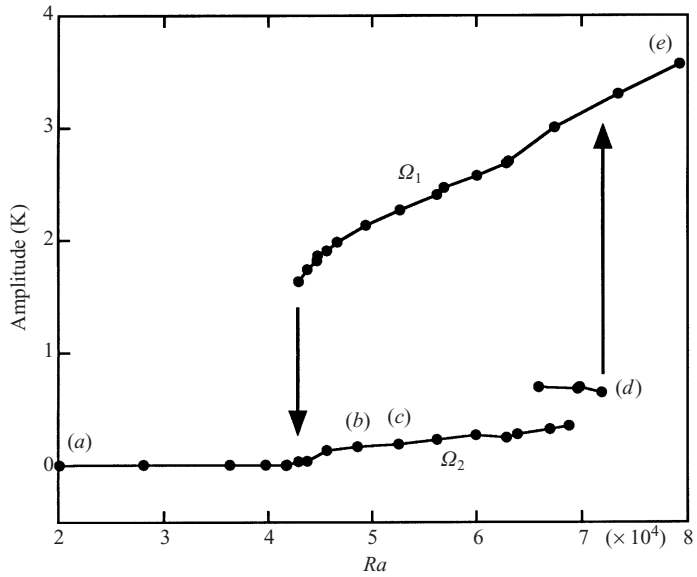

FIGURE 11. Amplitude of flow oscillations versus Ra at $T_m = 5.5 \times 10^4$. The letters (a)–(e) label flow states for which corresponding frequency spectra are shown in figure 12.

not in equilibrium, and the data qualitatively demonstrate the nature of the transitions. At $Ra = 3.8 \times 10^4$ the fluid makes the transition from steady flow to Ω_2 oscillations. As ΔT is further increased, the fluid motion evolves from singly periodic to more complex motions, and eventually becomes turbulent. At $Ra = 5.2 \times 10^4$, the fluid makes the transition to Ω_1 oscillations where the amplitude of the signal increases substantially. Buoyancy now dominates the flow and the signal is periodic with a harmonic at twice the dominant frequency. In this illustration, ΔT is continuously increased, and so the Ω_2 regime occurs first, followed by the Ω_1 regime. If ΔT were decreased instead, the Ω_1 oscillations would persist until the steady-state regime was reached.

The regimes identified in figure 2 define the flow nearest the steady regime. As the distance in T_m–Ra phase space increases from the steady regime, the flow patterns can change from those observed at the initial bifurcation point. As an example, we consider the bifurcation diagram for $T_m = 5.5 \times 10^4$, shown in figure 11. These data, unlike those shown in figure 10, were obtained with the steady-state measurement method. Referring to figure 2, the value of $T_m = 5.5 \times 10^4$ corresponds to where the dashed line demarcating the Ω_1–steady transition intersects the solid line demarcating the Ω_2–steady transition. That is, the lowest value of Ra for which Ω_1 oscillations exist upon decreasing Ra is the same as that where Ω_2 oscillations appear upon increasing Ra. The Ω_1 oscillations can clearly be distinguished from the Ω_2 oscillations. Not only are the frequency and relative phases of the signals different, as described above, but the amplitude of Ω_1 is approximately 10 times higher than the Ω_2 signal. The amplitudes of both oscillations increase for larger values of Ra. The letters (a)–(e) in figure 11 correspond to the respective frequency spectra shown in figure 12. The spectra all have the same scale with the exception of figure 12(e) which is shown at a higher scale. In the steady regime, figure 12(a), no oscillations are observed. Figure 12(b) is the spectrum corresponding to the Ω_2 oscillations. The bifurcation between the steady and Ω_2 regimes is characteristic of a supercritical Hopf bifurcation. The amplitude begins at zero and increases and the period is independent of Ra near

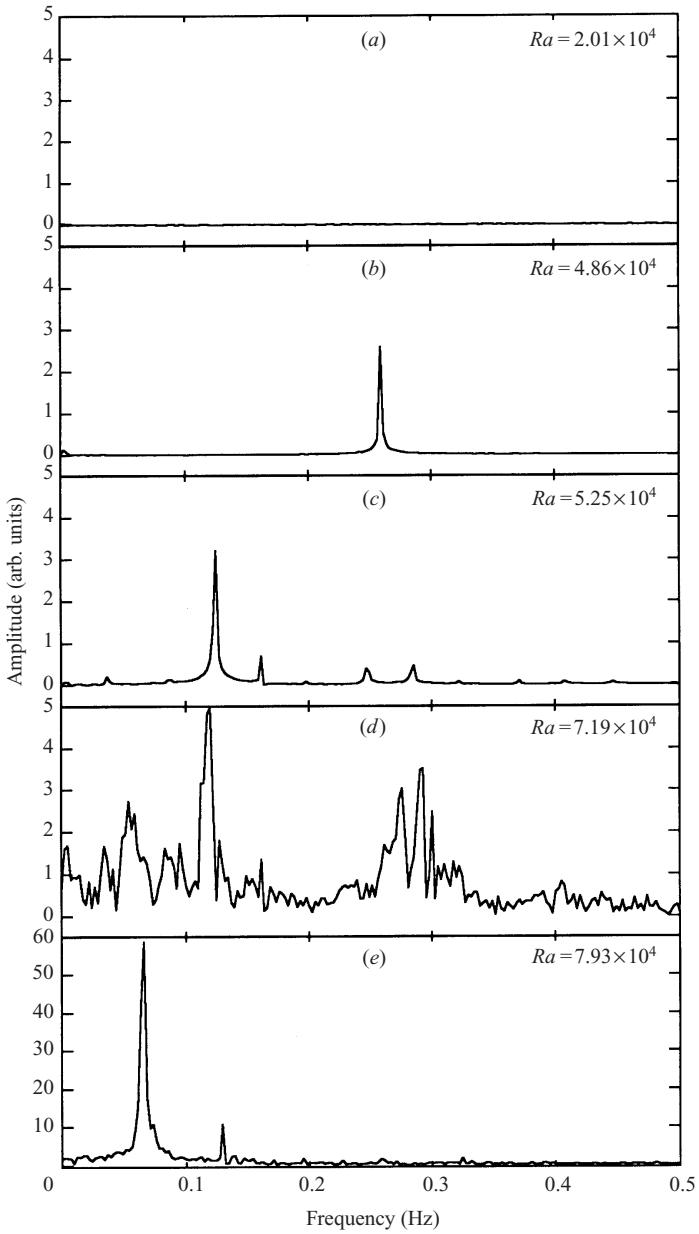

FIGURE 12. Frequency spectra of the flow states identified in figure 11. The data were obtained with $T_m = 5.5 \times 10^4$.

the bifurcation point. Between $Ra = 4.86 \times 10^4$ and 5.25×10^4, another bifurcation occurs. The amplitude does not change significantly but the signal is no longer singly periodic. The dominant period doubles as the frequency is changed from 0.258 Hz to 0.125 Hz. Between $Ra = 6.6 \times 10^4$ and 7.2×10^4 another flow regime exists which has a higher amplitude than the Ω_2 oscillations. This regime is non-periodic and a typical frequency spectrum is shown in figure 12(*d*). The range of values over which the transition to this regime occurred was between $Ra = 6.6 \times 10^4$ and 6.9×10^4. Above

$Ra = 7.2 \times 10^4$, the flow makes a transition to Ω_1 oscillations, a typical frequency spectrum for which is shown in figure 12(*e*).

4. Conclusions

The onset of time-dependent convection in liquid gallium subjected to both a destabilizing thermal gradient and a RMF has been experimentally investigated. At small values of Ra and T_m, a regime of stationary flow has been identified which is surrounded by several dynamically distinct regimes of time-dependent flow. The time-dependent flow regimes are identified both by the magnitude and relative phases of the frequency response of thermistors inserted into the melt. For small magnetic fields, Ra^c increases with increasing T_m, and the transition at Ra^c is observed to be a subcritical bifurcation. The hysteresis behaviour increases as T_m increases. An estimate of the induced fluid velocity can be obtained by comparing the present experiment with velocity measurements made by Barz *et al.* (1997) in a similar system. They reported azimuthal fluid velocities of a few mm s^{-1} for $T_m = 7.3 \times 10^4$. As $T_m^c = 1.5 \times 10^5$, it is apparent that a RMF can induce motion in fluid which is stationary with velocities on the order of mm s^{-1}. This is three orders of magnitude larger than typical semiconductor crystal growth velocities, which are on the order of $\mu m\, s^{-1}$. It thus appears that a RMF can be used to achieve the benefits of forced convection without triggering deleterious instabilities. A supercritical bifurcation to time-dependent flow does occur at T_m^c, and from a crystal growth standpoint it may be advantageous not to exceed this critical value.

This work was supported by the Microgravity Research Division of the National Aeronautics and Space Administration.

REFERENCES

Abricka, M., Krüminš, J. & Gelfgat, Y. 1997 Numerical simulation of MHD rotator action on hydrodynamics and heat transfer in single crystal growth processes. *J. Cryst. Growth* **180**, 388–400.

Barz, R. U., Gerbeth, G., Wunderwald, U., Buhrig, E. & Gelfgat, Y. M. 1997 Modelling of the isothermal melt flow due to rotating magnetic fields in crystal growth. *J. Cryst. Growth* **180**, 410–421.

Bergé, P., Pomeau, Y. & Vidal, C. 1986 *Order within Chaos.* John Wiley & Sons/Hermann.

Birat, J. P. & Choné, J. 1983 Electromagnetic stirring on billet, bloom and slab continuous casters: state of the art in 1982. *Ironmaking and Steelmaking* **10**, 269–281.

Brandes, E. A. & Brook, G. B. (Eds.) 1992 *Smithells Metals Reference Book*, 7th edn. Butterworth/Heinemann.

Brückner, F.-U. & Schwerdtfeger, K. 1994 Single crystal growth with the Czochralski method involving rotational electromagnetic stirring of the melt. *J. Cryst. Growth* **139**, 351–356.

Buell, J. C. & Catton, I. 1983*a* The effect of wall conduction on the stability of a fluid in a right circular cylinder heated from below. *J. Heat Transfer* **105**, 255–260.

Buell, J. C. & Catton, I. 1983*b* Effect of rotation on the stability of a bounded cylindrical layer of fluid heated from below. *Phys. Fluid* **26**, 892–896.

Chandrasekhar, R. S. 1961 *Hydromagnetic and Hydrodynamic Stability*. Oxford University Press.

Charlson, G. S. & Sani, R. L. 1971 On thermoconvective instability in a bounded cylindrical fluid layer. *Intl J. Heat Mass Transfer* **14**, 2157–2160.

Davidson, P. A. 1992 Swirling flow in an axisymmetric cavity of arbitrary profile, driven by a rotating magnetic field. *J. Fluid Mech.* **245**, 669–699.

Davidson, P. A. & Hunt, J. C. R. 1987 Swirling flow in a liquid-metal column generated by a rotating magnetic field. *J. Fluid Mech.* **185**, 67–106.

Dold, P. & Benz, K. W. 1997 Modification of fluid flow and heat transport in vertical Bridgman configurations by rotating magnetic fields. *Cryst. Res. Technol.* **32**, 51–60.

Dold, P. & Benz, K. W. 1999 Rotating magnetic fields: fluid flow and crystal growth applications. *Prog. Cryst. Growth Char. Mat.* **38**, 7–38.

Doronin, V. I., Dremov, V. V. & Kapusta, A. B. 1973 Measurement of the characteristics of the magnetohydrodynamic flow of mercury in a closed cylindrical vessel. *Magnetohydrodynamics* **9**, 412–413.

Fiederle, F., Eiche, C., Jörger, W., Salk, M., Senchenkov, A. S., Egerov, A. V., Ebling, D. G. & Benz, K. W. 1996 Radiation detector properties of $CdTe_{0.9}Se_{0.1}$:Cl crystals grown under microgravity in a rotating magnetic field. *J. Cryst. Growth* **166**, 256–260.

Fischer, B., Friedrich, J., Kupfer, C., Müller, G. & Vizman, D. 1999*a* Experimental and numerical analysis of the influence of a rotating magnetic field on convection in Rayleigh–Bénard Configurations. In *Fluid Mechanics and its Applications, Transfer Phenomena in Magnetohydrodynamic and Electroconducting Flows* (ed. A. Alemany *et al.*), pp. 279–294. Kluwer.

Fischer, B., Friedrich, J., Weimann, H. & Müller, G. 1999*b* The use of time-dependent magnetic fields for control of convective flows in melt growth configurations. *J. Cryst. Growth* **198/199**, 170–175.

Gelfgat, Y. M. & Gorbunov, L. A. 1994 Effects of alternating magnetic field on melt hydrodynamics in a cylindrical vessel with a free surface. *Magnetohydrodynamics* **30**, 237–247.

Gelfgat, Y. M., Gorbunov, L. A. & Kolevzon, V. 1993 Liquid metal flow in a finite-length cylinder with a rotating magnetic field. *Exps. Fluids* **15**, 411–416.

Iida, T. & Guthrie, R. I. L. 1988 *The Physical Properties of Liquid Metals*. Clarendon.

Kaiser, Th. & Benz, K. W. 1998 Taylor vortex instabilities induced by a rotating magnetic field: a numerical approach. *Phys. Fluids* **10**, 1104–1110.

Kamotani, Y., Weng, F. B., Ostrach, S. & Platt, J. 1994 Oscillatory natural convection of a liquid metal in circular cylinders. *J. Heat Transfer* **116**, 627–632.

Lide, D. R. (Ed.) 1999 *Handbook of Chemistry and Physics CRCnetBASE 1999*. CRC Press LLC.

Marty, Ph., Witkowski, L. M., Trombetta, P., Tomasino, T. & Garandet, J. P. 1999 On the stability of rotating MHD flows. In *Fluid Mechanics and its Applications, Transfer Phenomena in Magnetohydrodynamic and Electroconducting Flows* (ed. A. Alemany *et al.*), pp. 327–343. Kluwer.

Mößner, R. & Gerbeth, G. 1999 Buoyant melt flows under the influence of steady and rotating magnetic fields. *J. Cryst. Growth* **197**, 341–345.

Müller, G. & Neumann, G. 1983 Investigation of convective flows in model systems of directional solidification configurations. *Proc. 4th Eur. Symp. on Material Sciences under Microgravity, Madrid, Spain, 5–8 April 1983*. ESA SP-191, June 1983.

Müller, G., Neumann, G. & Weber, W. 1984 Natural convection in vertical Bridgman configurations. *J. Cryst. Growth* **70**, 78–93.

Neumann, G. 1990 Three-dimensional numerical simulation of buoyancy-driven convection in vertical cylinders heated from below. *J. Fluid Mech.* **214**, 559–578.

Priede, J. & Gelfgat, Y. M. 1998 Numerical simulation of the MHD flow produced by a rotating magnetic field in a cylindrical cavity of finite length. *Magnetohydrodynamics* **33**, 172–179.

Ramachandran, N. & Mazuruk, K. 1998 An experimental study of the effects of a rotating magnetic field on electrically conducting aqueous solutions. *First Pan Pacific Basin Workshop on Microgravity Sciences, Tokyo, Japan, 8–11 July 1998*.

Richardson, A. T. 1974 On the stability of a magnetically driven rotating fluid flow. *J. Fluid Mech.* **63**, 593–605.

Robinson, T. & Larsson, K. 1973 An experimental investigation of a magnetically driven rotating liquid-metal flow. *J. Fluid Mech.* **60**, 641–664.

Salk, M., Fiederle, M., Benz, K. W., Senchenkov, A. S., Egerov, A. V. & Matioukhin, D. G. 1994 CdTe and $CdTe_{0.9}Se_{0.1}$ crystals grown by the travelling heater method using a rotating magnetic field. *J. Cryst. Growth* **138**, 161–167.

Sorkin, M. Z. & Mozgirs, O. Kh. 1992 Controlling the structure of forced convective flow by means of rotating magnetic field inductors. *Magnetohydrodynamics* **28**, 202–205.

Spitzer, K. H., Dubke, M., & Schwerdtfeger, K. 1986 Rotational electromagnetic stirring in continuous casting of round strands. *Metall. Trans.* B **17B**, 119–131.

Spitzer, K. H., Reiter, G. & Schwerdtfeger, K. 1994 Volume force design in liquid metals by multifrequency electromagnetic stirring. *Intl Symp. on Electromagnetic Processing of Materials, Nagoya, Japan.* ISIJ.

Tiller, W. A. 1991 *The Science of Crystallization: Macroscopic Phenomena and Defect Generation.* Cambridge University Press.

Verhoeven, J. D. 1969 Experimental study of thermal convection in a vertical cylinder of mercury heated from below. *Phys. Fluids* **12**, 1733–1740.

Volz, M. P. & Mazuruk, K. 1996 Flow transitions in a rotating magnetic field. *Exps. Fluids* **20**, 454–459.

Volz, M. P. & Mazuruk, K. 1999 Thermoconvective instability in a rotating magnetic field. *Intl J. Heat Mass Transfer* **42**, 1037–1045.

Witkowski, L. M. & Marty, P. 1998 Effect of a rotating magnetic field of arbitrary frequency on a liquid metal column. *Eur. J. Mech.* B/*Fluids* **17**, 239–254.